Fe content effects on structural, electrical and magnetic properties of Fe-doped ITO polycrystalline powders

F.F.H. Aragón [a,*], J.A.H. Coaquira [a,b], S.W. da Silva [b], R. Cohen [c], D.G. Pacheco-Salazar [a], L.C.C.M. Nagamine [c]

[a] Laboratorio de Películas Delgadas, Escuela Profesional de Física, Universidad Nacional de San Agustín de Arequipa, Avenida Independencia s/n, Arequipa, Perú
[b] Núcleo de Física Aplicada, Instituto de Física, Universidade de Brasília, Brasília, DF 70910-900, Brazil
[c] Instituto de Física, Universidade de São Paulo, 05508-090 São Paulo, Brazil

ABSTRACT

Fe-doped indium tin oxide (ITO) is an exciting material because it combines the host matrix's good electrical conductivity with the magnetic properties coming from the most earth-abundant transition metal, Fe. In this regard, a single-pot synthesis route based on a polymeric precursor method has been used to produce high-quality undoped and iron-doped ITO with iron content up to 13.0 mol%. The crystal formation in the bixbyite-type structure of all samples is confirmed by X-ray diffraction data analysis. A monotonous decrease of the lattice parameters with the increase of the Fe content is determined, which is consistent with of Fe ions with an oxidation state of 3+ in agreement with the ionic radii difference between In^{3+} and Fe^{3+}. Raman spectroscopy confirms the bixbyite structure formation and provides evidence of a high surface disorder. ^{119}Sn Mössbauer spectroscopy reveals the formation of only Sn^{4+} ions. Meanwhile, ^{57}Co Mössbauer spectroscopy suggests the presence of Fe^{3+} ions in a paramagnetic state. DC magnetization characterization of the Fe-doped ITO nanoparticles confirms the compound's paramagnetic character. The sheet resistance (R/□) measurements provide a lower value for the undoped ITO sample (~0.26 Ω/sq) than the one of commercial bulk material. It has been determined that the sheet resistance increases with the Fe content, suggesting the decrease of the conduction electrons density as the iron content is increased.

© 2021 Elsevier B.V. All rights reserved.

1. Introduction

Nowadays, the focus on the production of transparent conductive metal oxides (TCMOs), nanostructures in the form of nanoparticles (NPs), thin films, nanowires, among others, are of extreme importance for technological applications because these materials combine their optical transparency in the visible region with their high electrical conductivity. One of the advantages of this system is its thermal stability at high temperatures until hundreds of Celsius degrees, making them a promising candidate for gas sensing devices [1], transparent contact in light-emitting diodes [2], photocatalytic degradation agent [3], and solar cells [4]. It is worth noticing that in the latter application, TCMOs films could act not only as a conducting surface but also as a junction [5]. Furthermore, the improvement of some above-mentioned applications can be intensified in nanoscale size. It is known that the semiconducting nature of the

transparent conductive metal oxide material is related to the deviations from the stoichiometric composition, which is intensified in the low dimensional systems, and the excess of oxygen vacancies can serve as electron donors. Chen et al. showed that the increase of oxygen vacancies develops a rise of bands below the Fermi level [6]. Indium tin oxide (ITO) is one of the most widely used transparent conducting oxides due to the good electrical conductivity (sheet resistance ~20 Ω/sq), and optical transparency around ~80% [7]. ITO crystallizes in the bixbite structure (with space group $Ia3$, T_h^7) the same as the indium oxide (In_2O_3) host lattice, which has 32 (In^{3+}) cations in the unit cell, and 48 (O^{2-}) anions. Eight of the In^{3+} atoms are located in the compressed InO_6 octahedra (*b*-site), with the In-O distance = 2.18 Å. The other 24 In^{3+} are placed in the high-disordered octahedra (*d*-site) with the In-O distances = 2.13, 2.19, and 2.23 Å [8,9]. To modify the physical and chemical properties of ITO powders numerous works in the literature have been used the doping process [10–13], in this regard, Fe-ions in one of the elements used as doping ITO in thin film [13,14] or nanoparticles [15,16] structure is a promising composite material due to combines the magnetic, optical and electric properties of the transition metal and oxide conductor,

producing a dilute magnetic semiconductor oxides (DMSOs), which is a potential for novel multifunctional material. In this respect, Chakraborty et al. claimed that the entry of the Fe ions into the ITO matrix of nanoparticle destroys the ferromagnetism (FM) [17]. Meanwhile, an opposite behavior was reported by Shao et al. for 2% Fe-doped ITO thin film, where the room temperature FM response is consistent with magnetic moment values higher than those reported for any iron oxides [14]. The latter evidence a knowledge gap specially related to the role played by the nanostructure in the final magnetic response.

In this work, we report a successful production of tin-doped In_2O_3 polycrystalline powders using a single-pot protocol based on a polymeric precursor method, which is indeed easy for scaling up. Additionally, the same protocol was successfully used to produce 10 mol% Sn-doped In_2O_3, and co-doped (10 mol% Sn, x mol% Fe) In_2O_3 nanoparticles, with x varying from 0 to 13 mol%. An experimental investigation was conducted to explore the structural, vibrational, magnetic, and hyperfine properties of In_2O_3, Sn-doped In_2O_3, and co-doped (10 mol% Sn, x mol% Fe) In_2O_3 NPs to contribute to the better understanding of the knowledge of doping TCMOs.

2. Experimental details

Nanoparticles of In_2O_3, ITO (10 mol% Sn-doped In_2O_3), and Fe-doped ITO in a range of 0–13 mol% were synthesized by the polymer precursor method (Pechine's method). Three hydrated indium nitrate ($In(NO_3)_3 \times 3H_2O$), citric acid ($C_6H_8O_7$), and ethylene glycol ($C_6H_8O_7$) were used to synthesize the undoped In_2O_3 polycrystalline powders. Concerning the doped samples, tin nitrate, and iron nitrate were used as metals precursors, both in predetermined concentrations. Subsequently, the obtained solution was thermally treated at 400 ºC for four hours to eliminate the organic remains present in the resultant sample in powder shape. Thereafter, it was milled using an agate pestle and mortar set. Subsequent thermal treatment at 500 ºC for 15 h was performed to warrant a good crystallinity of the samples. X-ray diffraction (XRD) measurements were performed using a Rigaku Ultima IV diffractometer with Cu-Kα radiation source (λ = 0.15418 nm) for structural characterization. Raman spectroscopy measurements were performed using a commercial triple spectrometer (Jobin Yvon, T64000) equipped with a charge-coupled device (CCD) detector. The Raman spectra were recorded in the wavenumber range of 200–800 cm^{-1}, varying the output power. Magnetic measurements were carried out using a commercial Physical Property Measurement System (PPMS) of the Quantum Design, in the range of temperatures 4–300 K, and applied magnetic fields up to ± 30 kOe. Both ^{119}Sn and ^{57}Co Mössbauer spectroscopy measurements were carried out to study the hyperfine properties at the Sn and Fe nuclei place, respectively. The Mössbauer spectra were fitted by minimizing the chi-square (χ^2) function, using the NORMOS software. The sheet resistances of the films were performed in pelletized powders thermal treated at ~1000 °C to guarantee the compaction for the electric measurements(with final dimensions of the pellet ~5 mm of diameter and ~0.5 mm of thickness) via the Jandel RM3000 test unit system.

3. Results and discussion

Fig. 1 exhibits the XRD patterns of the undoped, 10 mol% Sn-doped, and 10 mol% Sn, x mol% Fe co-doped In_2O_3 NPs collected from 2θ = 20º to 90º. The indexed lattice planes in all diffraction patterns are associated with the expected cubic bixbyite type phase (with space group Ia-3). No evidence of secondary crystalline phase was determined within the resolution limit of the technique. To obtain the structural parameters such as particle size, residual strain, and lattice parameter (a) as a function of the dopant-content Rietveld refinements of the XRD patterns were carried out. The Bragg
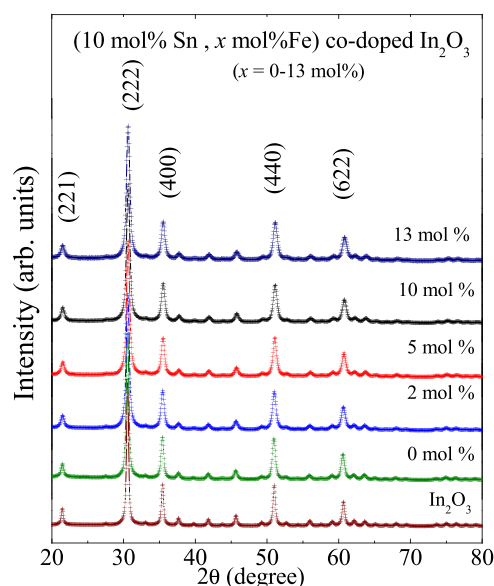

Fig. 1. X-ray diffraction patterns of the undoped In_2O_3 and (10 mol% Sn, x mol% Fe) co-doped In_2O_3 polycrystalline powders (with x varying from 0 to 13 mol%).

reflections peaks shape was modeled using the Lorentzian function implemented within the GSAS (General Structure Analysis System) software [18]. The full width at half maximum (β) was modeled using the following equation: β = $Ytan\theta$ + $X/cos\theta$ (where X and Y are refinement parameters). Assuming that the final linewidth (β) is related to the crystallite size and residual strain, the following relation can be used to evaluate both parameters:

$$\beta cos\theta = K\lambda/\langle D \rangle + 4\langle \varepsilon \rangle sin\theta \tag{1}$$

where $\langle D \rangle$ is the mean crystallite size, $\langle \varepsilon \rangle$ is the average residual strain and K is a dimensionless factor that depends on the particle shape ($K \sim$ 0.9 for a spherical shape). If one plots $\beta cos\theta$ as a function of $sin\theta$ (the Williamson–Hall plot), $\langle D \rangle$ and $\langle \varepsilon \rangle$ can be estimated from the data fit (see Fig. 2(b)). The lattice parameter found for the In_2O_3 NPs was a = 10.120 ± 0.005 Å, which is in good agreement with values reported in the literature (10.117 Å) [19]. Furthermore, the lattice parameter is increased about ~0.1% (a = 10.127 Å) after the doping with 10 mol% Sn (the ITO sample). Considering the substitutional process of In ions of the holding matrix by Sn ions, the increase of the lattice constant is inconsistent with Vegard's law, which predicts an unit cell reduction when smaller ions such as Sn^{4+}(0.69 Å) substitute larger ions such as In^{3+}(0.8 Å), both in VI-coordinated crystal sites. This unusual result is also reported by Nadaud et al. [9], and a plausible explanation could be related to the substitution of a cluster likely formed by one Sn^{4+} ion and one interstitial oxygen by one In^{3+} ion in the crystal structure [20], which leads to the observed unit cell expansion.

For the iron-doped ITO samples, the lattice parameter shows a slight increase for 1 mol% Fe, and after that, a decreasing behavior with the Fe content was determined, as shown in Fig. 2(c). It is known that the ionic radius of Fe^{3+} (0.785 Å) is smaller than the one of In^{3+} (0.8 Å), meanwhile, the ionic radius of Fe^{2+} (0.92 Å) is larger. Therefore, the lattice parameter's decreasing tendency can be attributed to the predominantly solid solution of Fe^{3+} ions in the ITO host matrix. Furthermore, the possibility of having Fe^{3+} ions in a low spin configuration cannot be ruled out. In that case, the 3+ iron ions are expected to have a smaller ionic radius (0.69 Å) in comparison to that one of In^{3+}. Mössbauer spectroscopy measurements can confirm these results as will be discussed below.

On the other hand, as displayed in Table 1, the residual strain determined for the 10% Sn-doped In_2O_3 sample, assessed via XRD data analysis, exhibited an increase when compared to the undoped
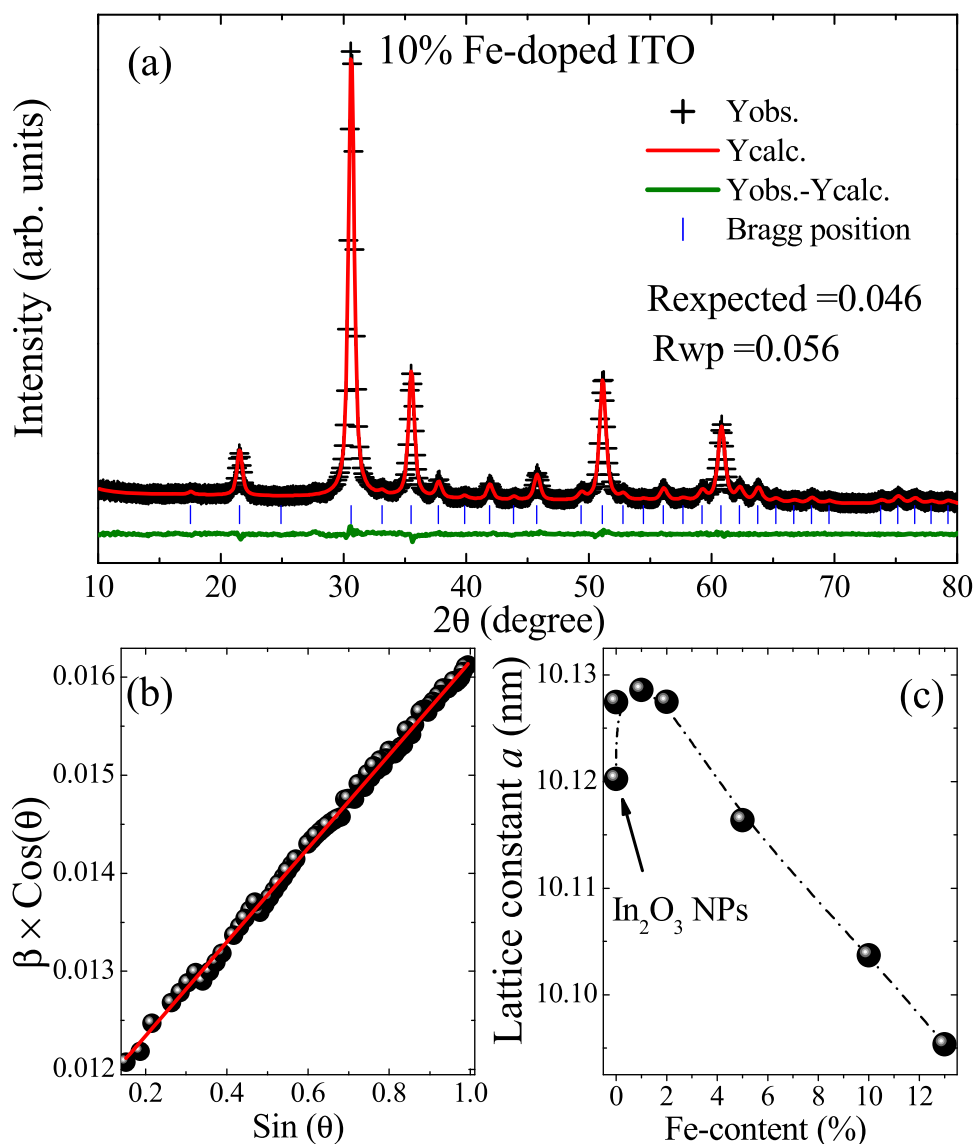
Fig. 2.(. a) Rietveld refinement obtained for the 10 mol% Fe-doped ITO NPs. The experimental data and the calculated data are represented by the points and the solid line, respectively, whereas the difference between them is represented by the line in the bottom part. (b) Williamson-Hall plot used to determine the crystallite mean size ($<D>$) and residual strain ($<\varepsilon>$) from the linear fit (solid line). (c) Lattice parameter dependence on the Fe content.

Table 1

Structural parameters obtained from the Rietveld refinement analyzes, where a is the lattice parameter, $<D>$ is the average crystallite size, $<\varepsilon>$ is the average residual strain, and S =R-wp/R-expected, parameter that quantifies the quality of the refinement.

Sample mol% Fe-doped ITO	a (Å)	$<D>$ (nm)	$<\varepsilon>$ (%)	S
In_2O_3	10.1202	22.7	0.06	1.02
ITO	10.1275	20.0	0.18	1.34
1	10.1286	14.0	0.09	1.27
2	10.1275	14.1	0.10	1.25
5	10.1164	13.5	0.08	1.25
10	10.1037	13.5	0.12	1.22
13	10.0954	13.5	0.18	1.23

sample. This fact suggests local deformations in the crystal lattice, induced by the presence of Sn^{4+} and interstitial oxygen atoms (as discussed above), which produce strongly strained (tensile and compressive) local regions. However, that scenario is passivated by the co-doping with iron contents up to 5 mol%. Above that concentration, the residual strain turns to increase again (see inset of Fig. 4(b)), which was found to be related to the high amount of

dopant ions. Regarding the size of the crystalline nanoparticles, as listed in Table 1, the introduction of dopant ions leads to a decreasing trend. It can be related to the progressive enrichment of iron ions at the particle surface as the iron content is increased, which reduces the surface energies and, therefore, decreasing the final particle size, in agreement with the Ostwald ripening equation [21].

Fig. 3 displays the room-temperature Raman spectrum for the In_2O_3 NPs using optical excitation of 1 mW. In agreement with the selection rules, 22 Raman-active (Γ = 4 A_g +4 E_g+14 T_g) modes are expected for the bixbyite structure of In_2O_3 [22]. However, as shown in Fig. 3, only 16 Raman modes were observed in the present work using the power mentioned above; meanwhile, six modes are commonly observed for similar samples in the literature at 109, 132, 306, 364, 496, and 627 cm^{-1}, which are a fingerprint for the cubic bixbyite In_2O_3 phase [8]. The very strong (vs) mode located at 132 cm^{-1} is assigned to the In-O vibration in the InO_6 octahedra. The other strong (s) mode located at 306 cm^{-1} is designated to the bending vibration of $\delta(InO_6)$ octahedra. The moderated mode at 364 cm^{-1} is assigned to the stretching vibrations of the In-O-In,
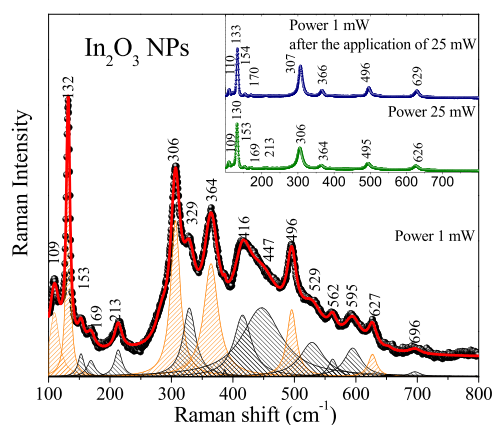
Fig. 3. Room-temperature Raman spectrum of the In_2O_3 NPs using optical excitation with 1 mW. In the inset, the Raman spectra performed at the same point of the sample are displayed, initially with a laser power of 25 mW and later with a laser power of 1 mW.

which is associated with oxygen vacancies in the In_2O_3 structure, meanwhile, the 496, and 627 cm^{-1} modes are attributed to the stretching vibrations of the same ν (InO_6) octahedral [8,23]. Other additional modes located at 153, 169, 213, 329, 416, 477, 529, 562, 595, and 695 cm^{-1} were also observed. To better understand the origin of the modes, additional measurements of Raman spectroscopy performed at the same point were carried out. Firstly, the laser power was increased to 25 mW, and a Raman spectrum was carried out. Subsequently, the laser power was reduced to 1 mW and another Raman spectrum was taken at the same point. Raman spectra obtained with 25 mW and subsequent reduction of power to 1 mW are shown in the inset of Fig. 3. As observed, only the peaks located at 109, 153, 169, 213, 132, 306, 364, 496, and 627 cm^{-1} were identified in both spectra. The observed differences between the Raman spectra obtained with 1 mW, before and after subjecting the sample to higher laser power (25 mW), suggest that the modes 329, 416, 477, 529, 562, 595, and 695 cm^{-1} only observed before subjecting the sample to higher laser power are induced by defects at the particle surface. These Raman modes were quenched because of the thermal treatment to which the sample is subjected during the measurements whit 25 mW.

A detailed list of all Raman modes' positions determined from the analysis is exhibited in Table 2. Room-temperature Raman spectra of In_2O_3 and ITO nanopowders are shown in Fig. 4(a), which shows the

redshift and broadening behavior of the vibrational modes after the tin doping. The latter is induced by strain provoke by the solid solution between Sn^{+4} and In^{3+}-ions, the formation of defects such as the tin-interstitial, tin-oxygen cluster, and oxygen vacancies (previously discussed), evidenced by the increase of the lattice parameter and the residual strain trend (see Table I). Fig. 4(b) exhibits the room-temperature Raman spectra of the Fe-doped ITO samples. As observed, the spectra display similar features as those determined for the In_2O_3 NPs, excluding the formation of secondary phases, in agreement with the results obtained from XRD data analyzes. Besides, analysis of the peak associated with the bending vibration of δ($InO6$) octahedrons (around 131 cm^{-1}) shows a redshift and peak broadening with the iron content up to 5%. After that, a blueshift and weakening of the Raman are determined. Those trends are consistent with that one determined for residual strain as shown in the inset of Fig. 4(b).

To study the local structure of the Sn ions room-temperature ^{119}Sn Mössbauer spectroscopy measurements were carried out for all Fe-doped ITO NPs at room temperature (see Fig. 5). A visual inspection of the Mössbauer spectra suggests the occurrence of only quadrupole electric interactions (doublets), as the result of the coupling between the nuclear quadrupole moment of the tin atoms and the non-zero electric field gradient in the matrix. Therefore, no evidence of supertransferred hyperfine field (STHF) from the Fe ions to nearby Sn ions have been found in the iron-doped ITO samples [24]. The spectra are well-resolved by considering two doublets (see Fig. 5) in agreement with the two crystalline sites occupied by tin ions in the bixbyite structure. During the fit process, the linewidth was fixed to $\Gamma = 0.84$ mm/s. The corresponding hyperfine parameters obtained from the fits are listed in Table 3. The fit of the spectrum of the undoped ITO NPs provided a quadrupole splitting (QS) and an isomer shift (IS) values of ~0.46 mm/s and ~0.13 mm/s, respectively, for the doublet 1 (D1), whereas $QS \sim 0.90$ mm/s and $IS \sim 0.13$ mm/s was determined for the doublet 2 (D2). It is determined that the IS of both sites do not show changes with the Fe content, meanwhile, the QS of D2 shows a slight increase from 0.90 to 1.04 mm/s for the 13 mol% Fe doped ITO sample. Moreover, according to the calculations reported by Yamada et al. [25], an electric field gradient of V_{ZZ} = 6.1×10^{17} Vcm^{-2} is determined for the d-site of Sn^{4+} ions; whereas a higher value of $V_{ZZ} = 12.1 \times 10^{17}$ Vcm^{-2} for the b-site of Sn^{4+} ions. Those calculations suggest that D1 and D2 could be correspond to tin ions occupying the d-site and b-site of bixbyite structure, respectively. Furthermore, from Mössbauer spectroscopy measurements, the intensity ratio of doublet 1 and 2 (D1/D2) provides information

Table 2

List of Raman modes for In_2O_3 and Fe-doped ITO obtained after the room temperature Raman spectra fit. The symbol * indicates that the measurement was made after the measurement carried out with a laser power of 25 mW at the same sample point.

In_2O_3 1 mw	In_2O_3 25 mw	In_2O_3 1 mw*	ITO	2% Fe doped ITO	5% Fe doped ITO	10% Fe doped ITO	13% Fe doped ITO	Assignment
109 w	109 w	109 w	109 w	108 w	107,w	109 w	109, w	In-O vibration of the InO_6 structure.
–	118 vw	119 vw						
132 vs	132 vs	133 vs	130 vs	130 vs	129 vs	131,vs	130, vs	Bending vibration of δ(InO_6) octahedrons.
153 vw	152 vw	154 vw	152 vw	151 vw		153 vw	152 w	
169 vw	169 vw	171 vw	170 vs	168 vs		170 vw		
213 w	211 vw	212 vw	217 w	215 w	215 w	215 w	216, w	
306 s	305 s	307 s	302 s	304s	302s	304 s	304, s	
329 m			330 w	333 w	333 w	332 w	334 w	Induced by surface
364 s	364 m	366 m	364 m	365 m	365m	365 m	365 m	ν (In-O-In)
416 m			419 w	416 w		418 w	419 w	Induced by surface
447 m, b			447 m, b	447 m,b	477m, b	477 m,b	477 m,b	Induced by surface
496 m	495 m	496 m	494 m	496 m	497m	497 m	498 m	ν(InO_6) octahedrons[23]
529 w						527 vw	530 w	Induced by surface
562 vw			562 vw			565, vw	566 vw	Induced by surface
595 vw						593, vw	595 vw	Induced by surface
627 w	626 m	629 m	626 m	627 m	630w	628 w	631 m	ν(InO_6) octahedrons[23]
696vw			694 w,b	697 w, b		697 w, b	699 w, b	Induced by surface

ν stretching, vs: very strong, s: strong, m: medium, w- weak, vw: very weak, b: broad.
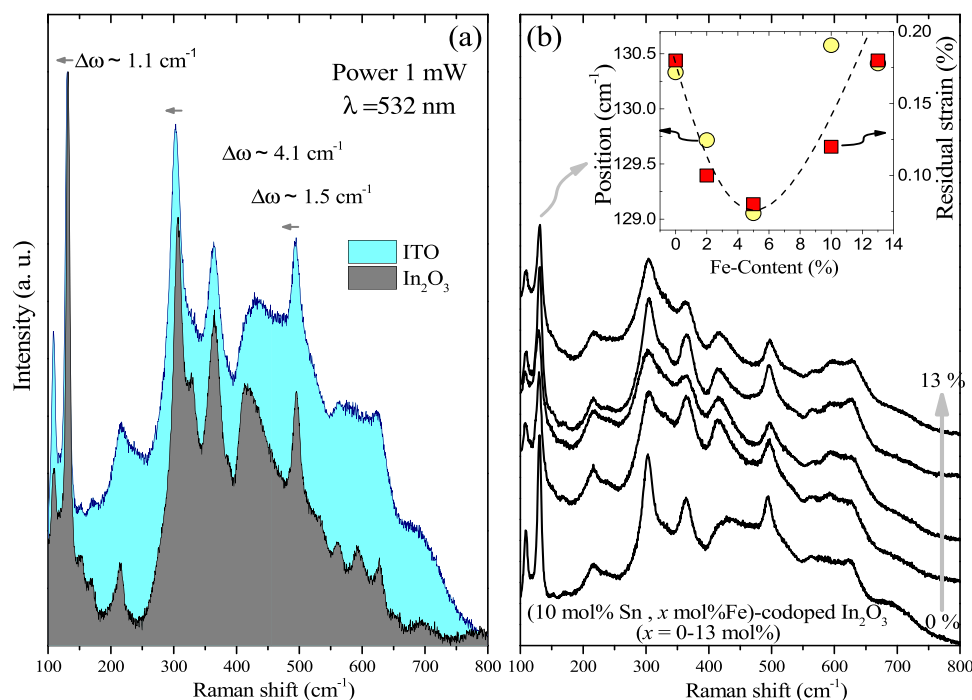
Fig. 4. (a) Room-temperature Raman spectra of the In_2O_3 and Sn-doped In_2O_3 (ITO) NPs using optical excitation of 1 mW. (b) And for Fe-doped ITO polycrystalline powders, the inset displays the Fe-content dependence of the bending vibration of $\delta(InO_6)$ octahedrons (around 131 cm^{-1}), and the residual strain obtained from XRD data analysis is also included. (For interpretation of the references to color in this figure, the reader is referred to the web version of this article.)
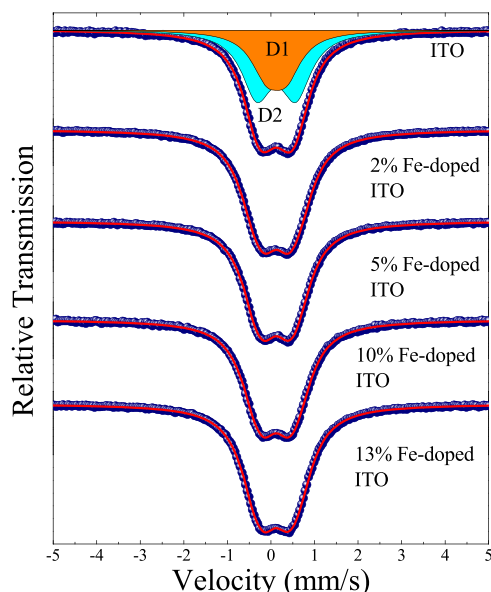
Fig. 5. Room-temperature Mössbauer spectra of the Fe-doped ITO NPs. The symbols represent the experimental data and the solid lines represent the fit.

Table 3
List of hyperfine parameters obtained from the Mössbauer spectra's fits: IS is the isomer shift, QS is the quadrupole splitting. The uncertainties are ± 0.01 mm/s for IS and QS and ± 0.1 for D1/D2 ratio.

Fe-content	Doublet 1		Doublet 2		
	IS (mm/s)	QS (mm/s)	IS (mm/s)	QS (mm/s)	D1/D2
0	0.13	0.46	0.13	0.90	~0.6
2	0.13	0.54	0.13	1.09	~1.7
5	0.13	0.52	0.13	0.97	~1.2
10	0.12	0.54	0.12	1.04	~1.6
13	0.12	0.52	0.13	1.04	~1.4

about the tin ions occupation in the crystalline sites. As can be seen in Table 3, the D1/D2 ~ 0.6 for the ITO sample, suggests a strong preference of Sn^{4+} ions for occupying *b*-site. After the Fe doping, the D1/D2 increases to 1.2–1.7, which depends on the Fe content, demonstrating that the presence of Fe ions provokes the redistribution of Sn ions in the cation sites of the bixbyite structure.

On the other hand, the hyperfine properties of the Fe impurities diluted in the indium tin oxide were also studied using ^{57}Co Mössbauer source for the 13% Fe-doped ITO NPs. Fig. 6(a) and (b) show the spectra obtained without applying a magnetic field at 300 K and 4.2 K, respectively. As observed, the spectra are well-resolved using two doublets(C1 and C2), indicating the absence of magnetic interactions among the magnetic moments of Fe ions, therefore, suggesting a paramagnetic behavior. The hyperfine parameters obtained from the fits are listed in Table 4. According to the literature, the hyperfine parameters are consistent with the presence of Fe^{3+}, which is in agreement with the XRD data analysis. To obtain more information about the magnetic response of Fe^{3+}ions, Mössbauer spectra in an external magnetic field (12 T) applied along the gamma-ray direction were carried out. Fig. 6(c) and (d) are shown the spectra obtained at 300 and 4.2 K, respectively. It is known that when a magnetic field is applied, the Mössbauer spectra show a magnetic splitting (sextet) and an effective magnetic hyperfine field can be determined from the spectra fit. That results from the sum of the applied magnetic field (H_{ext}) and the induced hyperfine field (H_{int}): $H_{eff} = H_{ext} + H_{int}$, where H_{int} is the hyperfine splitting (HS) contribution induced by the H_{ext}in the Fe nuclei at a specific temperature [26]. Measurement of the HS is correlated with the electrons polarization of the Fe ions on the ITO hold matrix. Previous reports in the literature showed that the HS is related to H_{ext}/T, according to the Brillouin function expected for a paramagnetic phase [26]. The H_{eff} values obtained from the fit of Mössbauer spectra are shown in Fig. 6(c) and (d). Accordingly, the estimated values of the internally induced contribution are $H_{int} \approx -0.2 T at 300 K$ and $+ 23.8 T$ at 4.2 K.The increase of H_{int} at low temperature is assigned to
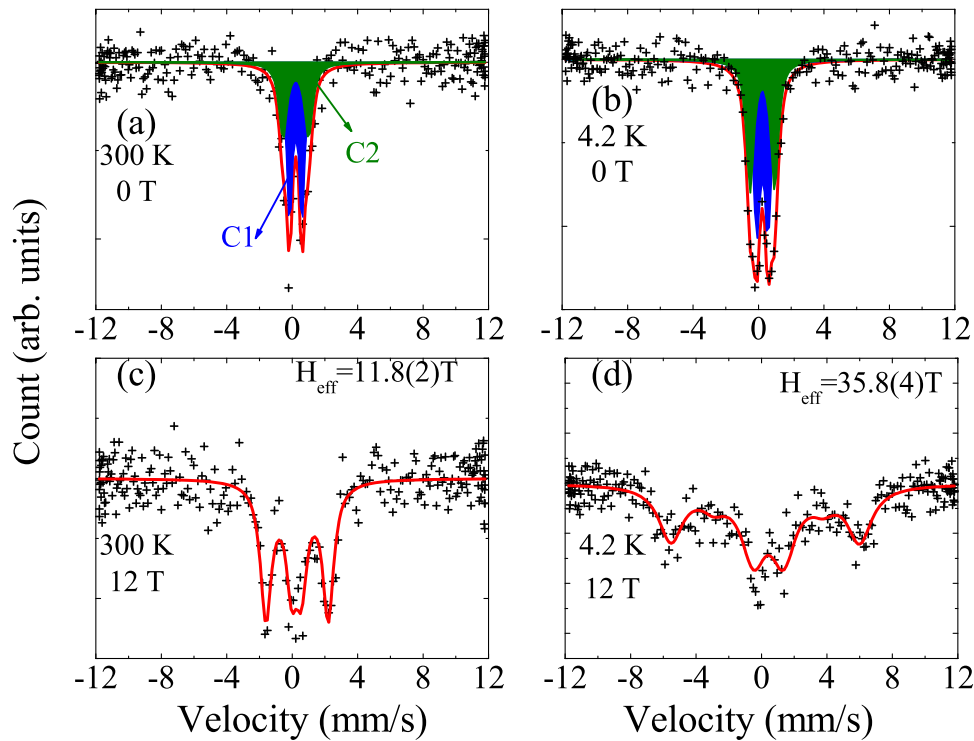
Fig. 6. ^{57}Fe Mössbauer spectra of the 13% Fe-doped ITO NPs at $T = 300$ K, (a) in zero magnetic field $B_{appl.} = 0$ T and (c) applied magnetic field, $B_{appl.} = 12$ T; at T = 4.2 K, (b) $B_{appl.} = 0$ T and (d) $B_{appl.} = 12$ T.

the dependence of the hyperfine splitting on the argument (H_{ext}/T) of the Brillouin function.

Fig. 7(a) and (b) show the magnetization (*M-H*) loops obtained at 300 and 5 K, respectively, for the Fe-doped ITO polycrystalline powders. As observed, the curves for all doped samples exhibit a linear trend at 300 K and saturating tendency at 5 K both compatible with a paramagnetic behavior coming from the magnetic ions dispersed in the diamagnetic matrix (ITO compound). To determine the thermal dependence of the magnetic properties magnetic susceptibility (χ) as a function of temperature curves were recorded in the range from 5 to 300 K and applying a magnetic field of 5 kOe (see Fig. 8). Data analysis confirms the paramagnetic behavior, in agreement with the *M-H* curves and the Mössbauer spectroscopy measurements performed at 300 and 4.2 K for the 13% Fe-doped ITO sample. Additionally, as shown in Fig. 8 χ vs.T curves were fitted to the Curie-Weiss law

$$\chi = \chi_0 + \frac{C}{T - \theta_{cw}} \qquad (2)$$

where *C* is the Curie constant, θ_{cw} is the Curie-Weiss temperature, χ_0 is the temperature-independent magnetic susceptibility [27]. The obtained parameters are listed in Table 5.

As seen in Table 5, θ_{cw} shows negative values for all samples suggesting the occurrence of antiferromagnetic interactions among the magnetic moments of iron-ions. Meanwhile, the Curie-Weiss temperature seems to become larger when the Fe content increases, indicating stronger antiferromagnetic coupling. Although the values

of the effective magnetic moment (μ_{eff}) obtained for all samples are dispersed, they are smaller than the expected value for spin-only contribution of free Fe^{3+} ions (5.9 μ_B) and they show a tendency to decrease as the Fe content is increased. The lower values found for the μ_{eff} can be assigned to with the short-range antiferromagnetic (AFM) correlation between spins of iron ↑↓.↑↓ dispersed in the host matrix, evidenced by the Curie-Weiss temperature's negative values, which drive to the reduction of the μ_{eff} (see Table 5). Likewise, the strengthening of AFM correlation evidenced by the more negative values of θ_{cw} as the Fe content is increased is consistent with the progressive effective magnetic moment decrease as observed in this work.

To determine the effects of the iron doping on the ITO matrix's electric transport properties sheet resistance (R/□) measurements using a standard four-point probe method were made, as described in the experimental part. Our results indicate that the undoped sample shows a lower sheet resistance value, R/□~0.26 Ω/sq, which is smaller than the value reported for the commercial ITO sample (~15–90 Ω/sq). This finding confirms the good crystalline quality of the samples studied in this work. After the Fe doping, the sheet resistance shows a monotonous increase as the Fe content is increased as shown in Fig. 9.

That sheet resistance increase could be associated with a decrease in the carrier concentration provoked by the Fe doping due to the carrier-type change from n-type to p-type as the Fe^{3+} content is increased. This result is in agreement with that reported in the literature for Fe-doped SnO_2 nanoparticles [28,29], wherein the

Table 4

List of hyperfine parameters obtained from the fit of ^{57}Fe Mössbauer spectra of the 13 mol% Fe-doped ISO sample. IS is the isomer shift, QS is the quadrupole splitting, Γ is the linewidth and A_{C1}/A_{C2} is the spectral area ratio of C1 and C2 subspectra.

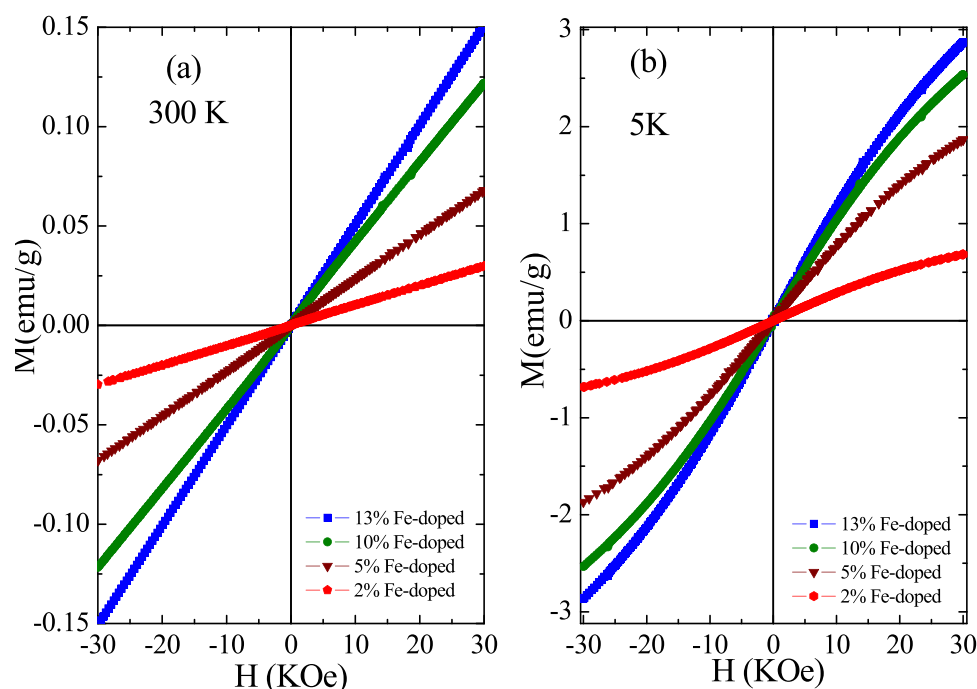| T(K)	C1			C2				
	IS(mm/s)	QS(mm/s)	Γ mm/s	IS (mm/s)	QS(mm/s)	Γ(mm/s)	A_{C1}/A_{C2}	X^2
300	0.22(1)	0.76(5)	0.44(7)	0.22(1)	1.50(9)	0.59(15)	1.5(9)	1.18
4.2	0.24(1)	0.70(9)	0.59(5)	0.24(1)	1.50(4)	0.59(5)	1.3(2)	1.05

Fig. 7. Magnetization (*M*) as a function of magnetic field (*H*) curves carried out at (a) 300 K and (b) 5 K for the Fe-doped ITO polycrystalline powders.
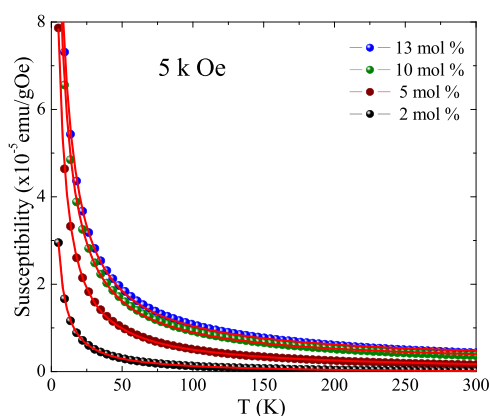

Fig. 8. Temperature-dependence of the magnetic susceptibility obtained for the Fe-doped ITO polycrystalline powders.

Fig. 9. Sheet resistance (R/□) as a function of the Fe content in the Fe-doped ITO polycrystalline powders.

Table 5
Parameters obtained from the data fit of the Curie- Weiss law relation for Fe-doped ITO polycrystalline powders.

x	C (× 10^{-5} emu.K/g.Oe)	θ_{cw} (K)	χ_0 (× 10^{-7} emu/g.Oe)	μ_{eff} (μ_B)
0.02	17.4 ± 0.1	−0.8 ± 0.1	−4.5 ± 0.8	4.33
0.05	50.3 ± 0.2	−1.4 ± 0.1	−0.6 ± 0.3	4.68
0.10	77.2 ± 0.5	−2.6 ± 0.1	14.4 ± 0.6	4.05
0.13	87.3 ± 0.7	−2.8 ± 0.1	18.9 ± 0.8	3.75

increase of the resistivity is related to Fe^{3+} or In^{3+} -ions located in interstitial positions, which would increase the 'hole concentration', driving to the decrease of the number of free electrons density, and consequently, to the sheet resistance increase.

4. Conclusions

In the present work, polycrystalline powders of indium oxide doped with 10% mol Sn (ITO) and indium oxide co-doped (Sn 10% mol, Fe) have been successfu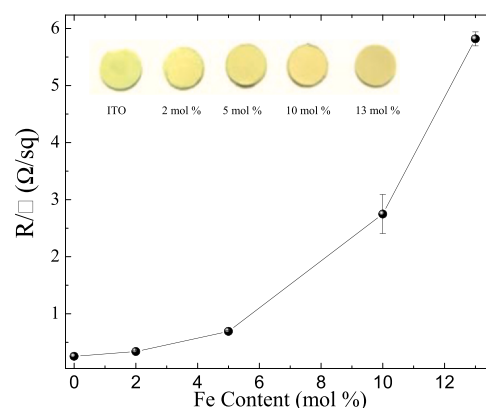lly synthesized by a polymer precursor method (from Fe varying from to 0–13 mol%). Analyzes of XRD data show bixbite monophase for all samples. Our findings show that the lattice parameter increases in ~0.1% of the ITO sample concerning the In_2O_3 sample. This fact is inconsistent with Vegard's law suggesting the formation of a different type of defect. However, for the Fe-doped ITO nanopowders, the lattice parameter decrease with the Fe content suggests a primary solid solution regime. The mean crystallite size decrease with the Fe content has been correlated with the iron surface enrichment on the particle surface region, which reduces the surface energy in agreement with the Ostwald ripening model. Laser power dependence of the Raman spectra of In_2O_3 and ITO nanopowders and a redshift and broadening behavior of the vibrational modes after the Sn doping evidence the presence of a high quantity of defects increased within ITO structure compared with the In_2O_3. Likewise, the shift of the powerful vibrational mode (~131 cm^{-1}) as the Fe content is increased has been correlated with the changes in the strain extent, which is in good agreement with the XRD measurements. Room-temperature ^{119}Sn Mössbauer spectroscopy measurements reveal the occurrence of strong electric quadrupole interactions in *b* sites rather than *d* sites, and no evidence of magnetic splitting is found for both sites. Meanwhile,

room-temperature 57Fe Mössbauer spectroscopy shows only a paramagnetic behavior. Magnetic measurements are consistent with the paramagnetic phase observed via Mössbauer spectroscopy measurements for the 13% Fe-doped ITO sample. Also, the progressive decrease of the Curie temperature has been correlated with the strengthening of the short-range antiferromagnetic correlations of iron ions as the iron content is increased.

CRediT authorship contribution statement

Fermin F.H. Aragón: Conceptualization, Methodology, Project administration, Investigation, Formal analysis, Data Curation, Supervision Investigation, Writing - original draft preparation, Writing - review & editing. **J.A.H. Coaquira**: Validation, Resources, Data Curation, Writing - review & editing. **R. Cohen**: Investigation and Data curation, Writing - review & editing. **D.G. Pacheco-Salazar**: Project administration, Data curation, Funding acquisition, Writing - review & editing. **L.C.C.M. Nagamine**: Investigation, Data curation, Funding acquisition, Writing - review & editing.

Declaration of Competing Interest

The authors declare that they have no known competing financial interests or personal relationships that could have appeared to influence the work reported in this paper.

Acknowledgments

References

[1] N.G. Patel, P.D. Patel, V.S. Vaishnav, Indium tin oxide (ITO) thin film gas sensor for detection of methanol at room temperature, Sens. Actuators B: Chem. 96 (2003) 180–189.

[2] K.-H. Ok, J. Kim, S.-R. Park, Y. Kim, C.-J. Lee, S.-J. Hong, M.-G. Kwak, N. Kim, C.J. Han, J.-W. Kim, Ultra-thin and smooth transparent electrode for flexible and leakage-free organic light-emitting diodes, Sci. Rep. 5 (2015) 9464.

[3] Y. Piña-Pérez, F. Tzompantzi-Morales, R. Pérez-Hernández, R. Arroyo-Murillo, P. Acevedo-Peña, R. Gómez-Romero, Photocatalytic activity of Al_2O_3 improved by the addition of Ce^{3+}/Ce^{4+} synthesized by the sol-gel method. Photodegradation of phenolic compounds using UV light, Fuel 198 (2017) 11–21.

[4] H. Hosono, Recent progress in transparent oxide semiconductors: materials and device application, Thin Solid Films 515 (2007) 6000–6014.

[5] H.B. Saim, D.S. Campbell, Properties of indium-tin-oxide (ITO)/silicon heterojunction solar cells by thick-film techniques, Sol. Energy Mater. 15 (1987) 249–260.

[6] A. Chen, K. Zhu, H. Zhong, Q. Shao, G. Ge, A new investigation of oxygen flow influence on ITO thin films by magnetron sputtering, Sol. Energy Mater. Sol. Cells 120 (2014) 157–162.

[7] J. Meyer, P. Görrn, T. Riedl, 17 - Transparent OLED displays, in: A. Buckley (Ed.), Organic Light-Emitting Diodes (OLEDs), Woodhead Publishing, 2013, pp. 512–547.

[8] J. Gan, X. Lu, J. Wu, S. Xie, T. Zhai, M. Yu, Z. Zhang, Y. Mao, S.C.I. Wang, Y. Shen, Y. Tong, Oxygen vacancies promoting photoelectrochemical performance of In_2O_3 nanocubes, Sci. Rep. 3 (2013) 1021.

[9] N. Nadaud, N. Lequeux, M. Nanot, Structural studies of tin-doped indium oxide (ITO) and $In_4Sn_3O_{12}$, J. Solid State Chem. 135 (1998) 140–148.

[10] M.J. Kim, J.H. Park, D.S. Jeon, T. Lee, T.G. Kim, Various metal-doped ITO as transparent conductive electrode for near-ultraviolet light emitting diodes, in: Proceedings of the 11th Conference on Lasers and Electro-Optics Pacific Rim (CLEO-PR), 2015, pp. 1–2.

[11] N.-W. Pu, W.-S. Liu, H.-M. Cheng, H.-C. Hu, W.-T. Hsieh, H.-W. Yu, S.-C. Liang, Investigation of the optoelectronic properties of Ti-doped indium tin oxide thin film, Materials 8 (2015) 6471–6481.

[12] X.H. Zhao, H.T. Li, S.W. Jiang, W.L. Zhang, H.C. Jiang, Effect of nitrogen doping on the thermoelectric properties of $ITO-In_2O_3$ thin film thermocouples, Thin Solid Films 629 (2017) 1–5.

[13] D. Chakraborty, S. Kaleemulla, No signature of room temperature ferromagnetism in Fe-doped ITO thin films, J. Supercond. Nov. Magn. 32 (2019) 729–737.

[14] Q. Shao, P.S. Ku, J.A. Zapien, C.W. Leung, A. Ruotolo, Nanostructured iron-doped indium tin oxide films: synthesis and characterization, IEEE Trans. Magn. 50 (2014) 1–4.

[15] D. Chakraborty, K.C. Kumar, S. Kaleemulla, I. Omkaram, Synthesis and characterization of Fe doped ITO nanoparticles, AIP Conf. Proc. 2221 (2020) 110001.

[16] A. Singhal, S.N. Achary, J. Manjanna, O.D. Jayakumar, R.M. Kadam, A.K. Tyagi, Colloidal Fe-doped indium oxide nanoparticles: facile synthesis, structural, and magnetic properties, J. Phys. Chem. C 113 (2009) 3600–3606.

[17] Deepannita Chakraborty, N. Madhusudhana Rao, G. Venugopal Rao, S. Venugopal Rao, S. Kaleemulla, C. Krishnamoorthi, Ferromagnetic and photoluminescence properties of Fe doped indium-tinoxide nanoparticles synthesised by solid state reaction, mechanics, Mater. Sci. Eng. 9 (2017) https://doi.org/10.2412/mmse.47.72.37 hal-01499399.

[18] B. Toby, EXPGUI, a graphical user interface for GSAS, J. Appl. Crystallogr. 34 (2001) 210–213.

[19] M. Marezio, Refinement of the crystal structure of In_2O_3 at two wavelengths, Acta Crystallogr. 20 (1966) 723–728.

[20] G. Frank, H. Köstlin, Electrical properties and defect model of tin-doped indium oxide layers, Appl. Phys. A 27 (1982) 197–206.

[21] A. Baldan, Review progress in Ostwald ripening theories and their applications to the γ′-precipitates in nickel-base superalloys Part II nickel-base superalloys, J. Mater. Sci. 37 (2002) 2379–2405.

[22] W.B. White, V.G. Keramidas, Vibrational spectra of oxides with the C-type rare earth oxide structure, Spectrochim. Acta Part A: Mol. Spectrosc. 28 (1972) 501–509.

[23] M. Kaur, N. Jain, K. Sharma, S. Bhattacharya, M. Roy, A.K. Tyagi, S.K. Gupta, J.V. Yakhmi, Room-temperature H_2S gas sensing at ppb level by single crystal In_2O_3 whiskers, Sens. Actuators B: Chem. 133 (2008) 456–461.

[24] S. Constantinescu, L. Diamandescu, I. Bibicu, D. Tarabasanu-Mihaila, M. Feder, Hyperfine interactions and dynamics characteristics of ^{119}Sn in $xSnO_{2-(1-x)}$α-Fe_2O_3 nanoparticle system, Hyperfine Interact. 184 (2008) 83–89.

[25] N. Yamada, I. Yasui, Y. Shigesato, H. Li, Y. Ujihira, K. Nomura, Doping mechanisms of Sn in In_2O_3 powder studied using 119 Sn Mössbauer spectroscopy and X-ray diffraction, Jpn. J. Appl. Phys. 38 (1999) 2856–2862.

[26] P.P. Craig, D.E. Nagle, W.A. Steyert, R.D. Taylor, Paramagnetism of Fe impurities in transition metals, Phys. Rev. Lett. 9 (1962) 12–14.

[27] K. Das, I. Ahmedmir, R. Ranjan, H.B. Bohidar, Size-dependent magnetic properties of cubic-phase MnSe nanospheres emitting blue-violet fluorescence, Mater. Res. Express 5 (2018) 056106(056101-056109).

[28] T.N. Soitah, C. Yang, L. Sun, Structural, optical and electrical properties of Fe-doped SnO_2 fabricated by sol–gel dip coating technique, Mater. Sci. Semicond. Process. 13 (2010) 125–131.

[29] M.M. Bagheri-Mohagheghi, N. Shahtahmasebi, M.R. Alinejad, A. Youssefi, M. Shokooh-Saremi, Fe-doped SnO_2 transparent semi-conducting thin films deposited by spray pyrolysis technique: thermoelectric and p-type conductivity properties, Solid State Sci. 11 (2009) 233–239.